Deciphering the Benefits of Coordinated Binders in Si-Based Anodes by Combined Operando/In Situ and Ex Situ X-Ray Micro- and Nano-Tomographies

Victor Vanpeene, Lucas Huet, Julie Villanova, Margie Olbinado, Federica Marone, Eric Maire, Lionel Roué, Thomas Devic, Bernard Lestriez

To cite this version:

Victor Vanpeene, Lucas Huet, Julie Villanova, Margie Olbinado, Federica Marone, et al.. Deciphering the Benefits of Coordinated Binders in Si-Based Anodes by Combined Operando/In Situ and Ex Situ X-Ray Micro- and Nano-Tomographies. Advanced Energy Materials, 2024, 10.1002/aenm.202403741 . hal-04710100

HAL Id: hal-04710100
https://hal.science/hal-04710100v1

RESEARCH ARTICLE

ADVANCED ENERGY MATERIALS
www.advenergymat.de

Deciphering the Benefits of Coordinated Binders in Si-Based Anodes by Combined Operando/In Situ and Ex Situ X-Ray Micro- and Nano-Tomographies

Victor Vanpeene, Lucas Huet, Julie Villanova, Margie Olbinado, Federica Marone, Eric Maire, Lionel Roué, Thomas Devic, and Bernard Lestriez*

The simple addition of a Zn(II) precursor to a preoptimized poly(carboxylic acid) binder solution enhances the electrochemical performance and cycle life of silicon-based electrodes. The binder/cation couple forms a cross-linked coordinated binder that plays a key role in enhancing the mechanical and chemical stability of the electrode microstructure. The impact of the addition of the Zn precursor on the microstructural evolution of the electrode during cycling is investigated at different scales (from cell/electrode to silicon particle scale) using complementary operando, in situ, and ex situ X-ray tomography techniques. Comparative analyses conducted on the reference and with Zn electrode formulations using operando and in situ X-ray micro-tomography allow for monitoring of the electrode morphological deformations along with the crack pattern formation and evolution during cycling. The benefits of the precursor addition include enhancing the mechanical stability of the electrode through a strengthened microstructure more apt to maintaining its integrity, as well as a better anchoring to the current collector leading to decreased electrical disconnections and capacity fade. Moreover, complementary ex situ X-ray nano-tomography measurements highlight the benefits of the precursor addition in terms of chemical stability with mitigated solid electrolyte interface (SEI) formation over the electrode cycling.

1. Introduction

In the current context of increasing battery energy density and stressing the need for higher-capacity negative electrode materials, the benefits, drawbacks, and proposed solutions to implementing silicon as an active material have already been thoroughly reviewed.[1–3] Its inherent large volumetric changes upon Si particle lithiation/delithiation lead to continuously destabilized electrode microstructure and solid electrolyte interface (SEI), which are evidenced through different degradation phenomena. In relation to the electrode mechanical properties, these include particle pulverization, film cracking, and delamination from the current collector resulting in electrical disconnections. When it comes to electrode chemistry, there is the continuous build-up of SEI, hindering the reaction kinetics and irreversibly trapping lithium. The combination of these

---

V. Vanpeene
Université Grenoble Alpes
CEA LITEN 17 rue des Martyrs, Grenoble 38054, France
E-mail: victor.vanpeene@cea.fr

V. Vanpeene, J. Villanova
ESRF- The European Synchrotron
Grenoble F-38000, France

L. Huet, T. Devic, B. Lestriez
Institut des Matériaux Jean Rouxel (IMN)
CNRS UMR 6502
Université de Nantes
Cedex 3, Nantes F-44322, France

The ORCID identification number(s) for the author(s) of this article can be found under https://doi.org/10.1002/aenm.202403741

DOI: 10.1002/aenm.202403741

L. Huet, L. Roué
Institut National de la Recherche Scientifique (INRS)
Centre Énergie
Matériaux, Télécommunications (EMT)
1650, boulevard Lionel Boulet, Varennes, QC J3X1P7, Canada

M. Olbinado, F. Marone
Swiss Light Source
Paul Scherrer Institute
Villigen 5232, Switzerland

E. Maire
INSA Lyon
MATEIS
CNRS UMR 5510
Villeurbanne F-69621, France

effects leads to continuous capacity fade and early electrode failure. To prevent these issues, common approaches aim to tailor the active material architecture and composition,[1] optimize the electrolyte composition and additives,[4] and improve the electrode mechanical properties through binder optimization.[4–6]

Reinforcing the electrode mechanical properties through binder reticulation and/or cross-linking is a promising route toward a more resilient electrode microstructure.[7] Different mechanical behaviors of Si-based anodes will arise depending on the nature of this reticulation. For example, supramolecular interactions (e.g., hydrogen bonds) are associated with low bonding strength but could lead to partial/improved recovery properties whereas covalent cross-linking could lead to higher cohesion strength, but poor reversibility.[8] Cation–ligand coordination bonds between the organic chains, which are of intermediate strength and reversible, appear here to be a promising alternative. Specifically, such a reticulation does not require specific, tailor-made organic compounds, but can rely on the simple addition of a metallic salt to an already-mastered binder formulation with a polymer chain bearing complexing groups such as carboxylates which are commonly found in Si binders. Initially, the beneficial impact of such a coordinative reticulation on the electrode mechanical properties was observed through a so-called "maturation process," that leads to binder cross-linking through Cu(II) ions from the corroded current collector, resulting in matured electrodes with greater resistance to cracking and delamination.[9,10] The enhanced mechanical properties of the cross-linked carboxymethylcellulose (CMC) binder have been further confirmed by simple addition of $CuSO_4$[11] and more recently $ZnSO_4$ and ZnO additives to the electrode formulation[12,13] Overall, the addition of Zn^{2+} ions to the binder has been shown to further cross-link the carboxylate moieties through coordination bonds, enhancing mechanical properties such as the cohesion of the composite film, as well as the Young's modulus and hardness. The latter two were even maintained in the presence of carbonate-based solvent (most likely due to restricted polymer chain mobility when coordinated). The coordinated binder also acts to some extent as an artificial SEI in the resulting electrodes, reducing electrolyte degradation. Moreover, the Zn was not electrochemically active as evidenced by STEM-HAADF imaging of the pristine and aged states.[14] Thus, the use of coordinated binders has been shown to mitigate both most prominent degradation mechanisms in silicon composite electrodes. However, the underlying mechanism improving the capacity retention is yet to be fully understood from both a mechanical and chemical points of view, but especially in terms of the dynamical process at the beginning of the electrode cycling.

Laboratory and synchrotron X-ray tomography have received increasing interest over the past decades for research in battery materials science due to increasing spatial resolution and data quality, along with high throughput data acquisition.[15,16] Moreover, tomography data are no longer limited to qualitative insights but have been complemented by quantitative analysis,[17] especially supported by the improvement in temporal resolution through operando and in situ capabilities, and the development of new analytical approaches and tools.[18] In this context, a multiscale and multimodal approach is proposed to address the issues with accelerating battery characterization,[19] especially in the case of Si-based electrodes.[20] In the present study, such a multiscale correlative approach is proposed for deciphering the benefits of a coordinated binder in Si-based anodes by bridging the micro- and nano-scales with X-ray synchrotron tomography as illustrated in **Figure 1**. The focus is on the comparison of two binder formulations, a reference NaCMC binder and its counterpart coordinated through to the addition of a Zn(II) salt. Operando-interrupted analyses performed during the first and third cycles of the different cells at two different scales were used to monitor the dynamical electrode deformation, cracking, and gas evolution. Representative in situ (in-cell) and ex situ analyses were also used for high-resolution imaging of the cracking pattern and SEI evolution over cycling to gain a deeper understanding of the long-trend evolution over the early cycle life of the electrode (25 cycles). These observations highlight the benefits of the coordinated binder both on the mechanical properties through a stiffer and more resilient electrode structure and on the chemical properties by mitigating SEI build-up.

2. Results and Discussion

2.1. Electrode Formulation and Corresponding Electrochemical Performance

The ink formulations are based on two different aqueous binder solutions, each mixed with silicon powder and conductive additive in mass ratios close to 70/10/20 wt% (silicon/graphene/binder).[12] The reference binder solution (without Zn) is composed of sodium carboxymethylcellulose (NaCMC) dissolved in a buffer solution of citric acid (CA) and potassium or sodium hydroxide (NaOH/KOH) at the desired pH of 3–3.5.[11] For the binder solution with Zn, the Zn(II) precursor is added to reach a previously optimized molar coordination ratio of $Zn/RCO_2H = 0.22$. For comparison, two different precursors ($ZnSO_4$ and ZnO) were studied using each characterization method, but only the most noteworthy results obtained with the $ZnSO_4$ salt are presented in the main text, referred to as the "with Zn" formulation. Characterizations of the ZnO formulation can be found in the supplementary information (Figures S1–S3, Supporting Information). For the electrochemical performance assessment, electrodes with a diameter of 3 mm and an active mass loading of 1.75–2.0 mg_{Si} cm^{-2} were selected. For the sake of representativeness, the same electrode diameter was chosen for electrochemical performance tests and X-ray tomography investigation. Complementary data with more representative electrodes of 1 cm in diameter and with longer cycling (60 cycles) have already been reported in our previous work. We can therefore confirm the superior cycling performance of the Zn-based formulation and that the diameter of the cell has a minor influence on the electrochemical results.[12] **Figure 2a** shows the evolution of the specific capacity over cycling of electrodes with the reference binder compared to those containing Zn additive. The capacity retention of the electrodes with the Zn coordinated binder is superior to those with the reference binder, ≈2550 and 1520 mAh g_{Si}^{-1} after 25 cycles, respectively. Note that intermediate values of 2000 mAh g_{Si}^{-1} are measured after 25 cycles for the formulation with ZnO (Figure S1, Supporting Information). This trend aligns with the results obtained for 1 cm diameter electrodes cycled in "traditional" Swagelok cells in otherwise similar cycling conditions. Note that the effect of the current collector on the capacity

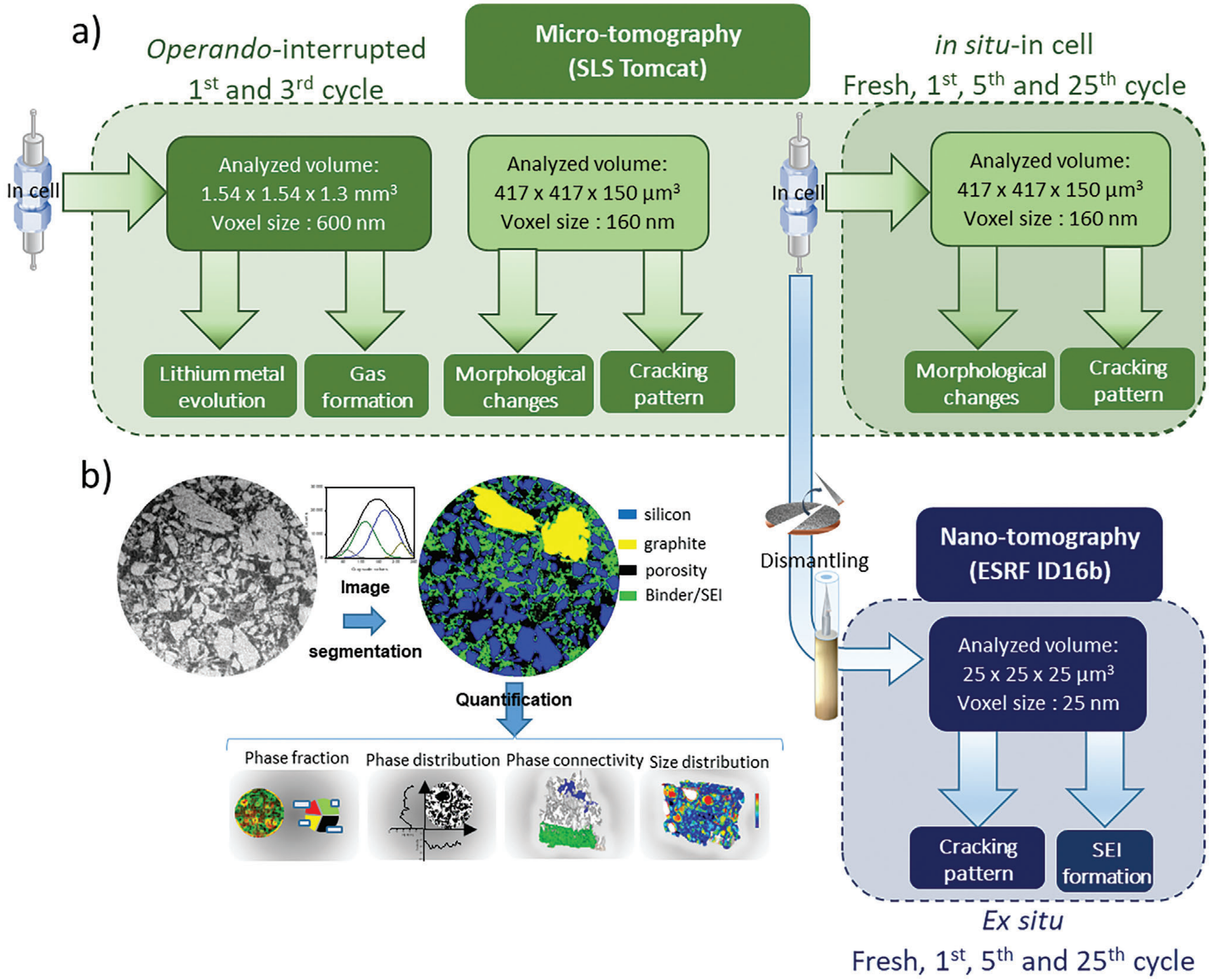

Figure 1. a) Illustration of the multimodal and multiscale X-ray tomography analysis workflow and b) procedure for quantitative image analysis.

retention can be significant, especially in the case of the reference formulation as is briefly discussed in the Figure S2 (Supporting Information) and in our previous work.[13] Figure 2b shows the evolution of the coulombic efficiency over cycling for the reference and with Zn electrodes. The trend in these formulations' performances is similar in terms of the specific capacity with Zn being superior to without Zn. Interestingly, the first cycle CE is of the same order of magnitude as the CE obtained in "traditional" Swagelok cells, ≈80%. Figure 2c,d show the evolution of Si anode voltage as a function of the cell capacity for the reference and with Zn formulations, respectively, for selected cycles of interest, i.e., 1st, 5th, and 25th.

The superior electrochemical performance for the silicon composite electrodes containing Zn likely comes from a denser and more stable SEI coupled with improved electrode mechanical properties. Qualitative evidence of the formation of a better (i.e., denser and more stable) inorganic SEI after the first cycle was gathered through ex situ STEM-EDX.[14] Further, a variety of mechanical characterization highlighted improved mechanical properties, indicating that the with Zn electrodes were more resistant to fracturing in their initial state.[12] These interesting initial observations require operando and in situ characterization over multiple cycles to better understand the improvements brought on by binder coordination. This can only be done through synchrotron X-ray tomography.

2.2. X-Ray Tomography Analysis

The X-ray tomography analyses were performed at the micro- and nano-scales for *(i)* operando, *(ii)* in situ in-cell, and *(iii)* ex situ conditions for the reference and with Zn formulations. *(i)* Operando-interrupted measurements over the 1st and 3rd cycles were conducted with 0.16 and 0.65 µm voxel sizes. Both resolutions are essential in order to observe the dynamical changes of the electrode's microstructure with precision (volume of 417 × 417 × 150 µm^3), as well as the dynamical evolution at the half-cell level including the lithium electrode, separator with

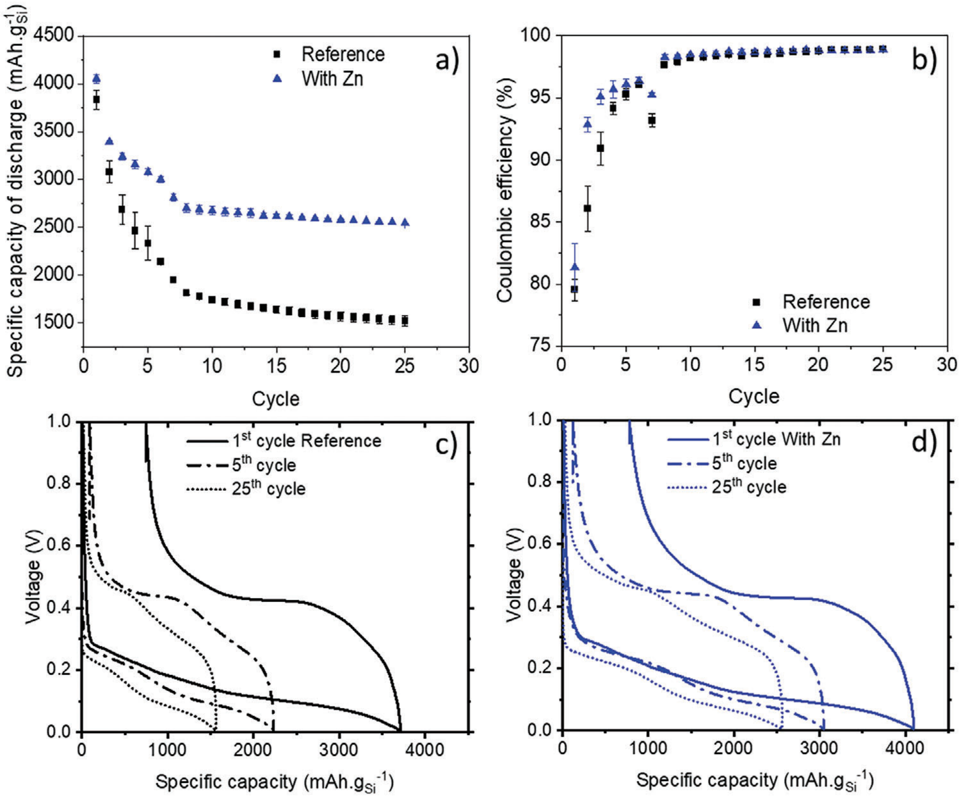

Figure 2. a) Mean specific discharge capacity and b) coulombic efficiency as a function of cycle number for the reference (in black) and with Zn (in blue) formulations. The mean capacity and standard deviation values were determined using 5 cells for each formulation. Voltage versus capacity curves for cycles 1st, 5th, and 25th for c) the standard formulation and d) with Zn. The C-rate was C/40 for the first cycle, C/20 for the next 5 cycles, and C/10 for the subsequent cycles.

electrolyte, and Si anode (volume of 1.54 × 1.54 × 1.30 mm^3). *(ii)* In situ "in-cell" 3D images with a voxel size of 0.16 µm were taken of different cells after the 5th and 25th cycles, respectively. Cell assembly is based on a previously developed set up.[21] *(iii)* Nano-tomography was performed ex situ in sub-volumes extracted from the just above-mentioned cells with a pixel size of 25 nm. This is illustrated by the workflow scheme in Figure 1. For further details about the different methods and conditions, see the experimental/methods section.

2.2.1. Electrode Morphological Changes Along Its Cycle Life

Figure 3 illustrates the morphological changes in the reference (a–c) and with Zn (d, e) electrodes through cross section (a and d) and in-plane (b and e) in-cell X-ray micro-tomography images (0.16 µm voxel size). The separator is visible on top and the Cu current collector on the bottom of the cross-section images. Higher magnification images obtained by ex situ X-ray nano-tomography are presented below for the standard formulation (c) and with Zn (f). At the initial state, barely any differences in microstructure are visible in either the micro-tomography or the high magnification images between formulations. Secondary particles of 1–3 µm diameter, graphene sheets (indicated with yellow arrows), and pores can be distinguished in the presented 25 × 25 $µm^2$ regions (Figure 3c,f). The porosity volume fractions measured by image processing are comparable: 35 and 37$\%^v$ for the reference and with Zn formulations, respectively. After the 1st cycle, the electrode is massively cracked and an irreversible thickness that increases with further cycling expansion is already observed for both formulations with higher amplitude for the reference formulation (Figure 3a,c; Figure S3, Supporting Information). As cycling continues, the electrode cracks tend to close, and its structure appears to get progressively less dense (darker grey scale level indicates lower mass density). This is observed sooner (5th cycle) for the reference formulation with a more abrupt irreversible volume expansion evolution. Interestingly, the cracking dynamics at the particle scale are different from at the electrode scale as depicted by the high-resolution nano-tomography images that will be discussed in detail in the next section.

The operando-interrupted acquisitions allow tracking of the electrode/separator interface displacement during lithiation/delithiation, giving access to the relative electrode thickness variation as shown for the 1st and 3rd cycles in **Figure 4a,b** for both formulations. The corresponding lithiation/delithiation videos show the cross-section images of the half-cell stack during the 1st and 3rd cycles, illustrating the electrode expansion/contraction (Video S1, Supporting Information for the reference formulation and Video S2, Supporting Information with Zn). During electrode lithiation, the thickness increase is linear as previously reported in literature.[10,20,22–24] However, a short delay is noticeable for the reference formulation with its

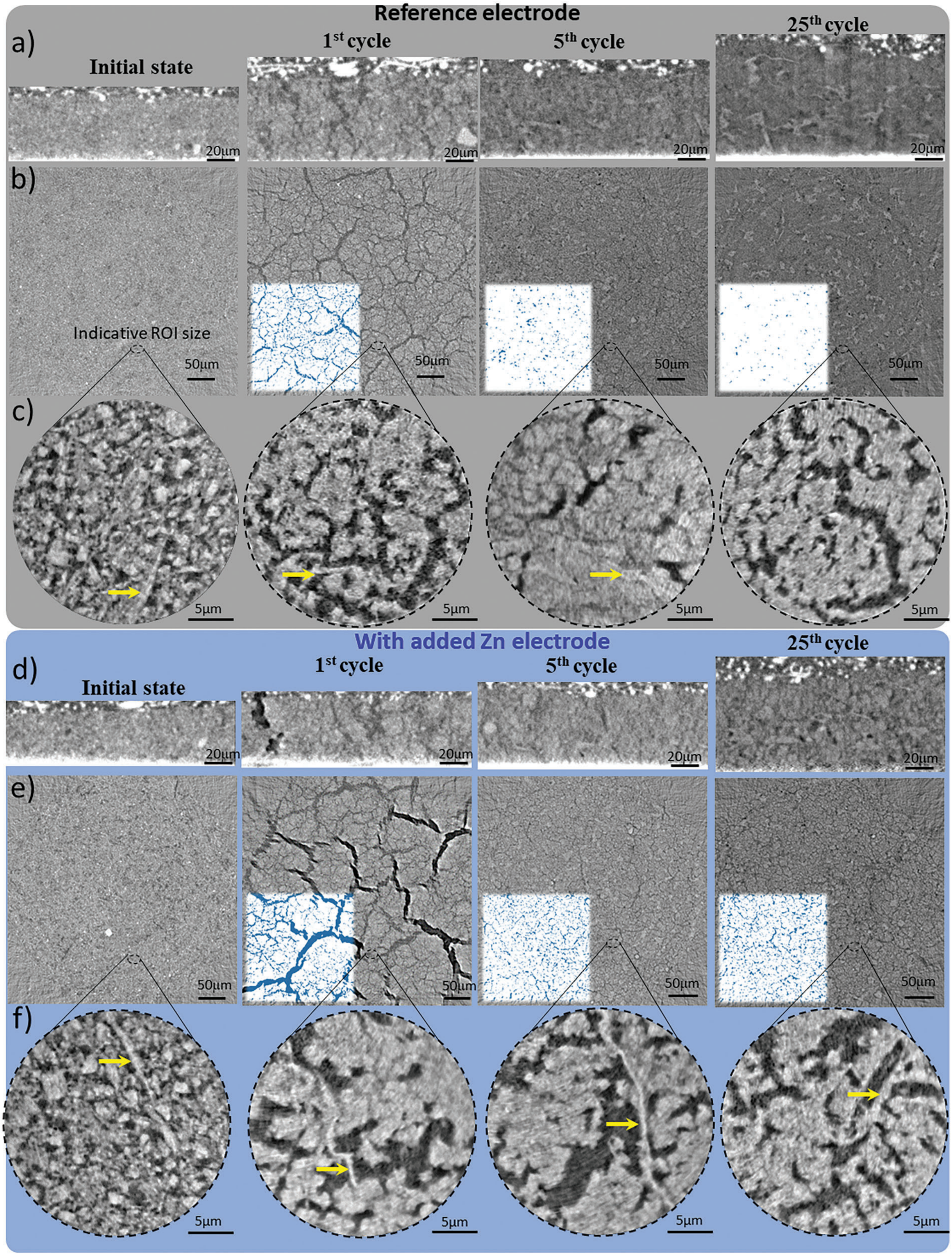

Figure 3. Reconstructed tomographic images a,b,d,e) at a 0.16 µm voxel size (a and d: cross section, b and e: in plane at mid-height) and c,f) X-ray nano-tomography reconstructed images at a 25 nm voxel size for the a–c) reference and d–f) with Zn formulations. From left to right: at the initial state, end of the 1st, 5th, and 25th cycle. Insert images of segmented cracks labeled in blue are overlaid on in-plane images. Yellow arrows indicate graphene sheets.

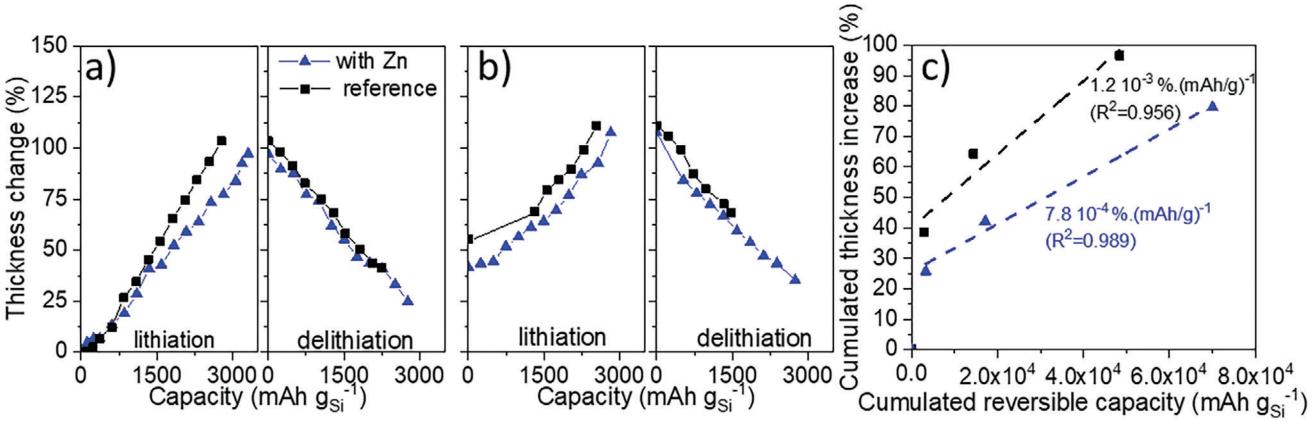

Figure 4. Thickness expansion (along the z axis) of the electrode for the reference (in black) and with Zn (in blue) formulation, a) for the 1st and b) 3rd cycle. c) Cumulated electrode thickness increase as a function of the cumulated reversible capacity.

thickness increasing after 250 mAh g_{Si}^{-1}. Moreover, the thickness expansion slope for the standard formulation (not shown) is slightly steeper than for the formulation with Zn, namely 0.04 versus 0.03% (mAh g_{Si}^{-1})$^{-1}$, underlining its greater tendency to dilate. The maximum expansions measured at the 5 mV cut-off voltage are of 103% and 97% for the reference and with Zn formulations, respectively. The values are quite similar but the with Zn electrode had a higher capacity (+500 mAh g_{Si}^{-1}). Expansion values can be normalized with respect to their lithiation capacity according to Equation (1):

$$\overline{\Delta h} = \frac{\Delta h \times C_{th}}{C_{exp}} \tag{1}$$

where $\overline{\Delta h}$ and Δh are the normalized and measured thickness expansions, C_{th} and C_{exp} being the theoretical (3579 mAh g_{Si}^{-1}) and measured capacities, respectively. For the 1st lithiation (delithiation) the capacity measured for the formulation with Zn was equal to 3303 (2764) mAh g_{Si}^{-1}, hence the coulombic efficiency was 83.7%. In comparison, the measured capacity for the reference formulation was significantly lower with 2779 (2238) mAh g_{Si}^{-1} after the 1st lithiation (delithiation) and a corresponding coulombic efficiency of 80.5%. Taking this into account, the difference in thickness expansion is more marked with normalized values of 133% (mAh g_{Si}^{-1})$^{-1}$ and 105% (mAh g_{Si}^{-1})$^{-1}$ for the reference and with Zn electrodes, respectively. Interestingly, the reference electrode normalized thickness expansion value is close to the theoretical expansion of 148% estimated using Equation (2):

$$\Delta h_{el}\,[\%] = \emptyset_{m,Si} \times \frac{\rho_{theo}}{\rho_{Si}} \times \Delta V_{Si}\,[\%] \times Q_{Si} = 0.0533 \times Q_{Si} \tag{2}$$

where $\phi_{m,Si}$ is the Si mass fraction in the pristine electrode (0.732), ρ_{theo} is the calculated true density of the pristine electrode (2.17 g cm^{-3}),[23] ρ_{Si} is the true density of Si (2.33 g cm^{-3}), ΔV_{Si} is the intrinsic volume expansion of $SiLi_x$ (0.0782% per mAh g_{Si}^{-1} as its expansion is of 280% for x = 3.75 or 3579 mAh g^{-1}),[25] and Q_{Si} is the measured electrode capacity (mAh g_{Si}^{-1}). In comparison, the gap is greater for the formulation containing the Zn-coordinated binder with a 105% normalized thickness expansion compared to the theoretical 171% expansion. These observations highlight the difference in mechanical properties between formulations as previously reported with scratch tests and nanoindentation methods. In fact, the mechanical properties of the electrode coatings saturated with propylene carbonate were previously measured by nanoindentation for the with Zn and reference formulations. They had hardness values of 50–65 versus 15–20 MPa and elastic moduli of 3–4.5 versus 1–1.5 GPa, respectively.[12] Subsequently, during delithiation, the electrodes contract and reach a residual thickness expansions of 42 and 25% at the 1 V cutoff voltage equivalent to an expansion of +17 and +10 µm for the reference and with Zn electrodes respectively (Figures 3a,c, and 4a). The normalization with respect to their reversible capacity, i.e., 67% and 32%, exacerbates this difference and indicates a somewhat better mechanical resistance of the formulation with Zn after one cycle.

For the 3rd cycle, the measured capacities in lithiation (delithiation) are 2537 (1329, incomplete) and 2818 (2740) mAh g_{Si}^{-1} for the reference and with Zn formulations, respectively. At the beginning of the 3rd cycle, the residual true thickness increases are of 55 and 42%, respectively (Figure 4b), underlining the progressive swelling of the electrode that is mitigated by the Zn-coordinated binder. The maximum thickness expansions measured after the 3rd lithiation are 111% and 108% (156 and 137% with respect to normalized capacity), highlighting a still limited microstructure swelling in the formulation with Zn at the 3rd cycle despite a higher operational capacity. This observation holds after further cycling as shown in Figure 4c based on in-cell measurements performed on different batteries. The cumulated irreversible expansion, estimated from each electrode's initial thickness as measured prior to cycling, is +27.8 (+16) µm, +42 (+35) µm after the 5th and 25th cycles, respectively, for the reference (with Zn) formulation (Figure 3). Hence, the cumulated residual expansion reaches nearly 100% after 25 cycles for the reference electrode, whereas it is limited to 80% for the electrode with the Zn-coordinated binder. Interestingly, the microstructure resiliency is superior for the with Zn formulation despite having the highest reversible capacity after 25 cycles (2500 mAh g_{Si}^{-1} versus 1560 mAh g_{Si}^{-1} for the reference formulation) and therefore the largest expansion/contraction of the silicon phase among the tested formulations. The thickness evolution trends are clearly different between the two formulations with a 1.5-fold expansion rate (in % per mAh g_{Si}^{-1}) for the reference formulation. These observations indicate better constraint of the overall dimension of the anode when zinc cations are added to induce polymeric binder cross-linking. This is also supported by our previous reports using other methods[9,10,12] and by other groups working with reticulated binders.[26,27] Since then, sensitivity measurements conducted using discrete approaches implemented in a contact-based mechanical model have shown that the irreversibility in the electrode swelling comes mainly from the adhesion work force, which corresponds to the binder network strength.[28] This underlines once more the importance of the mechanical properties of the binder in enhancing the mechanical stability of the Si composite electrode microstructure during cycling.

2.2.2. Dynamical Evolution of the Cracking Pattern

Qualitative Image Observation for In-Cell and Ex Situ Observations: The non-destructive nature of X-ray tomography allows for visualization of the electrode crack patterns at different steps of cycling. On one hand, the driving force for the appearance of these cracks is the volume change of the active phase (silicon) upon lithiation (expansion) and delithiation (contraction). This driving force is quite similar for both types of electrodes (i.e., reference and with Zn), particularly during the first cycles where their electrochemical capacities are nearly the same. On the other hand, resistance to the propagation of these cracks is an intrinsic property of the composite material constituting the observed anodes. We would like hereafter to highlight that this intrinsic property is strongly modified by the addition of zinc as a binder cross-linking agent to the formulation.

Note that in the reconstructed images shown above, some cracks are filled with electrolyte (dark grey regions in Figure 3) while others are filled with gas (black regions in Figure 3). The subsequent analysis was carried out after segmenting the cracks regardless of the nature of the phase inside the crack. Looking at the in-plane sections of the electrode films after the 1st cycle (Figure 3b,e), a standard mud-cracking behavior is observed for both kind of electrodes. As previously reported in literature,[9,13,29] the formation of islets of electrodes separated by wide cracks is observed. However, the electrode islets are twice as big in the electrode with Zn (ca. 40 × 40 μm^2) than in the reference electrode (ca. 20 × 20 μm^2). Those islets contain multiple narrower cracks, constituting a complex, ramified pattern. **Figure 5** presents the 3D rendering images of the largest interconnected clusters of cracks at the different cycling stages observed by "in-cell" and ex situ X-ray micro-tomography (a, c) and nano-tomography (b, d) scans of different cells. These two measurements are complementary as they allow us quantifying the crack network formed at different scales. After the 1st cycle, the cracking patterns are already qualitatively different between the two formulations, which remains the case during their respective evolutions over cycling. At first, the electrode formulated with Zn has a network of large, interconnected cracks which leave internal islets, each containing a different set of interconnected, smaller cracks (visible on the higher resolution images of Figure 5d). In contrast, the reference formulation has a network of smaller, fully interconnected cracks spanning through the whole electrode. The absence of voids in the upper-right corner (Figure 5a) is believed to arise from the volume boundaries. With further cycling, the cracks progressively decrease in width as the cumulated volume expansion keeps increasing for both formulations. Visually, it is clear that the Zn additive is characterized by the preservation of a well interconnected crack network still visible on both scales over cycling (Figure 5c,d).

Quantitative Image Analysis for Operando Observations: The segmented images (see materials & method and supplementary information for more details) of the cracks formed in the electrodes during the operando-interrupted measurements at 160 nm pixel size were used to calculate the corresponding volume fraction, surface over volume ratio, mean width (using the local thickness tool[30] implemented in ImageJ), and crack network interconnectivity (estimated from the ratio of the largest intra-connected volume of crack over the crack total volume). These measurements are summarized in **Figure 6** and supported by videos of the operando-interrupted cross sections along with lateral views of the electrode/separator and electrode/current collector interfaces during the first delithiation of the reference (Video S3, Supporting Information) and with Zn electrodes (Video S5, Supporting Information). The first cracks form at 1050 mAh g_{Si}^{-1} (28% of electrode contraction) for the former and 750 mAh g_{Si}^{-1} (30% of electrode contraction) for the latter. Note that this is an estimation because there is a 30 min gap between acquisitions corresponding to roughly 6% (equivalent to ≈240 mAh $g^{-1}{}_{Si}$) of electrode contraction. Decreasing this gap would increase the precision but also increase the total duration of the measurement on the beamline. At this stage, the corresponding volume fractions of cracks are 1.6%^{v} and 2.9%^{v}, the surface over volume ratios are 1.6 and 1.8 μm^2 μm^{-3}, and the mean crack widths are 0.9 and 1.61 μm for the reference and with Zn electrodes, respectively (Figure 6a–c). As the delithiation progresses and the electrodes contract, the cracks propagate throughout the entire electrode film, all the while the volume fraction of cracks is progressively increasing, which is associated with a clear crack widening (Figure 6a,c). At the end of the 1st cycle, the crack volume fraction and mean width values are substantially higher for the Zn-based electrode (24%^{v} and 2.4 μm vs 16%^{v} and 1.9 μm) while the surface over volume ratio of its crack network is reduced compared to the reference electrode at 0.67 versus 0.90 μm^2 μm^{-3} (Figure 6b), indicating wider cracks for the electrode with Zn. These results can be correlated to the observations made here above for the in-cell measurements. After the advent of the first cracks in the formulation with Zn, the crack surface over volume ratio drops drastically and then reaches a plateau. The evolution of this ratio is more progressive in the reference electrode (Figure 6b). At this point (red arrow), the crack surface increases again, demonstrating the formation of new, smaller cracks (see also Video S5, Supporting Information) in the Zn electrode. On the other hand, the reference electrode does not show any secondary threshold as its surface/volume ratio is continuously decreasing in a smoother way, which depicts a gentler broadening of the cracks along with the apparition of new cracks of similar dimension (see also Video S3, Supporting Information). This suggests two different cracking mechanisms. On one hand, the electrode with Zn releases its mechanical energy accumulated during

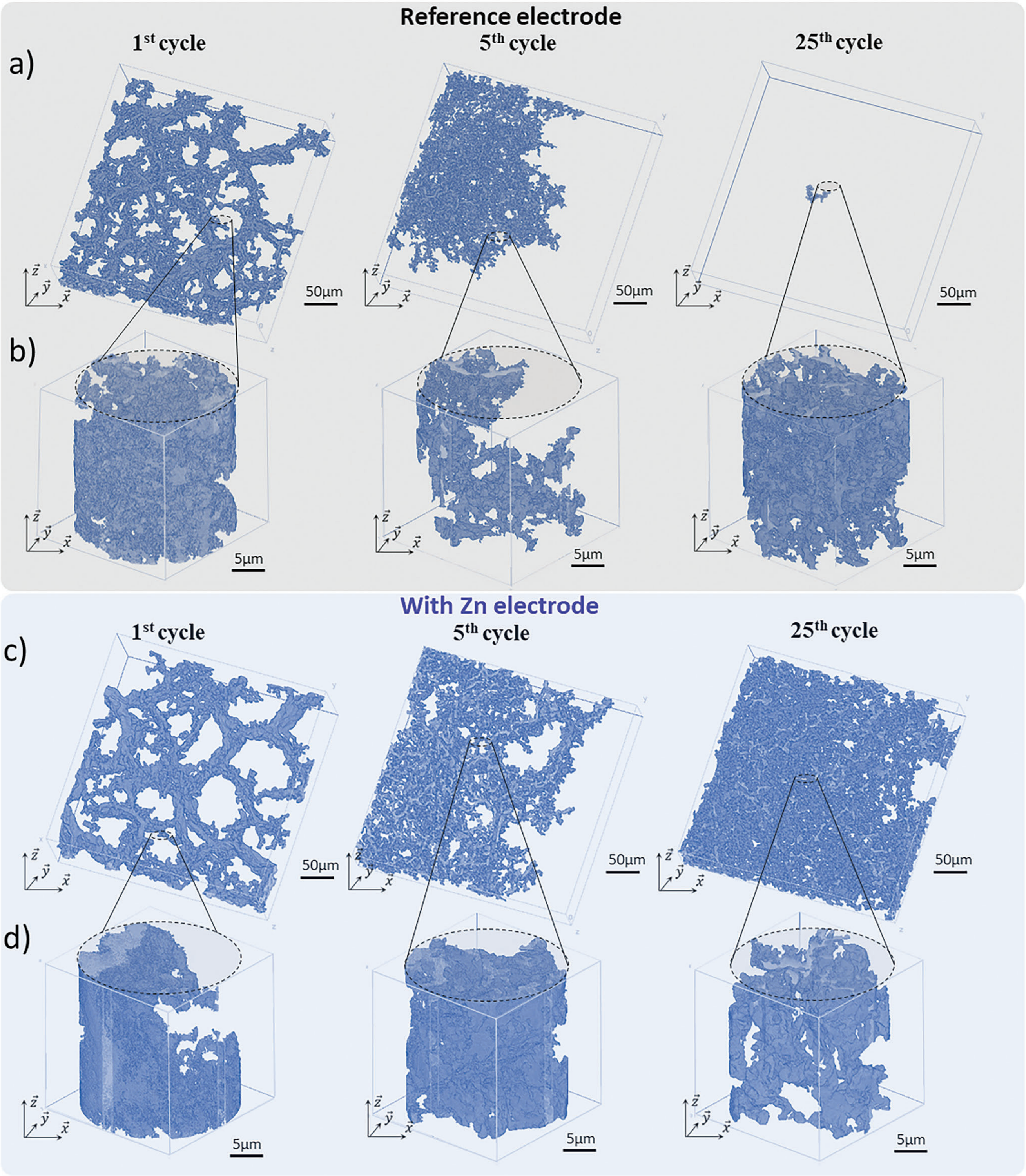

Figure 5. 3D rendered images of the largest interconnected volumes of cracks for the reference a,b) and with Zn c,d) formulations taken from different electrodes stopped at different steps of cycling. From left to right: end of the 1st, 5th, and 25th cycle. Close up views b,d) from ex situ nano-tomography ($25 \times 25 \times 25$ µm^3) are displayed below each image.

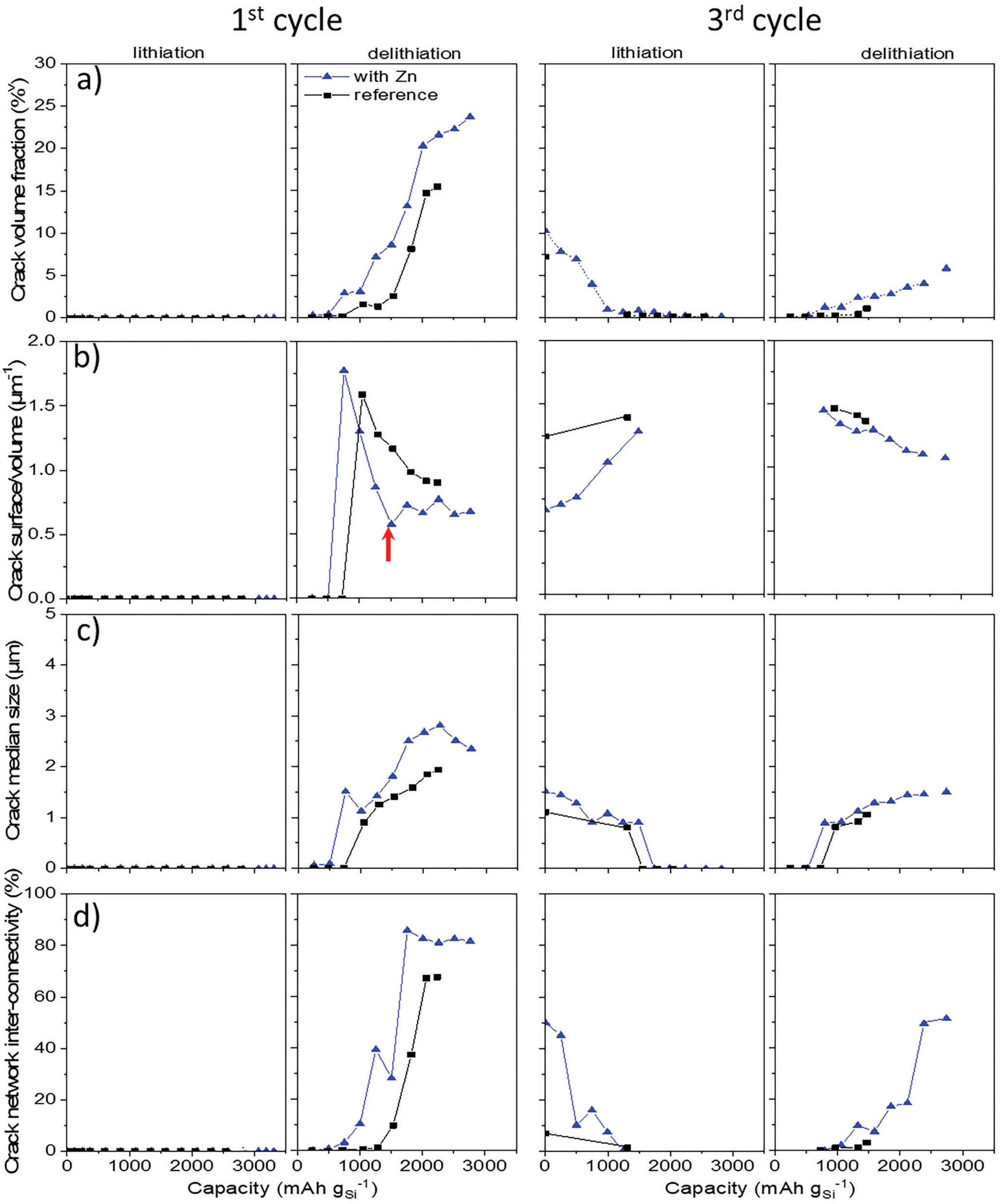

Figure 6. Evolution of a) the crack volume fraction, b) crack surface over volume, c) crack median width, and d) crack network interconnectivity during the 1st and 3rd cycles of the reference (in black) and with Zn (in blue) electrodes. Note that no acquisitions were possible for the reference formulation electrode after 1500 mAh g_{Si}^{-1} of the 3rd delithiation due to the beam time ending.

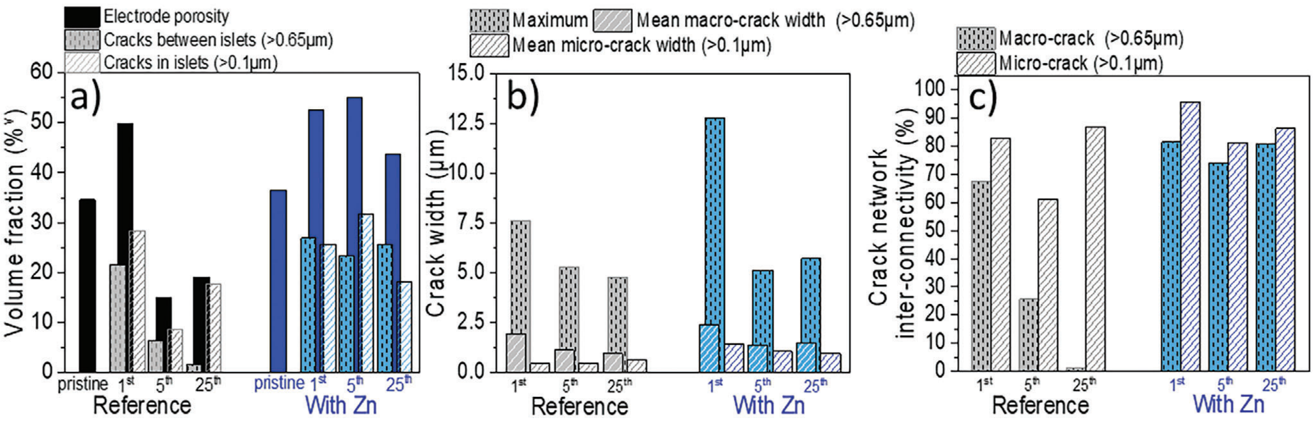

Figure 7. a) Crack and porosity volume fraction, b) crack width, and c) crack network interconnectivity as a function of the cycle number for the reference (in black) and with Zn (in blue) electrodes. Macro- and micro-cracks correspond to analyses done in volumes of 417 × 417 × 150 µm^3 (resolution >0.65 µm) and 25 × 25 × 25 µm^3 (resolution >0.1 µm), respectively.

delithiation through few but wide cracks with a relatively small total surface area. On the other hand, the reference electrode continuously creates new cracks leading to a network of numerous, narrow cracks and resulting in high tortuosity and relative total surface area. This higher reactive surface promotes further electrolyte decomposition and SEI formation and ultimately larger cumulative volume expansion. This is clearly visible on the 3D rendering images of Figure 5a,c and particularly highlighted by the differences measured in their crack interconnectivity, equal to 67% for the reference electrode compared to more than 85% for the Zn one (Figure 6d).

After the second cycle, the overall crack volume fraction of both electrode formulations has gone down to 7 (reference) and 10%^{v} (with Zn) as compared to 15 and 24%^{v} at the end of the 1st cycle, along with a high remaining interconnectivity of 50% for the with Zn electrode versus 7% for the reference one (**Figure** 6a,d). This shows a more pronounced closing of the crack network in the case of the electrode without coordinatively reticulated binder. For the Zn formulation, the crack surface over volume ratio is practically identical to the value reported at the end of the 1st delithiation, i.e., 0.66 versus 0.67 µm^2 µm^{-3}, whereas this value has drastically increased for the reference with 1.25 versus 0.9 µm^2 µm^{-3} (Figure 6b). During the next delithiation, the crack network retains most of its characteristics (volume fraction, mean width, interconnectivity) for the with Zn electrode. Note that no were possible for the reference formulation electrode after 1500 mAh g$_{Si}$$^{-1}$ of the 3rd delithiation due to the beam time ending.

Quantitative Image Analysis of the "In-Cell" and Ex Situ Images: To complete the previous analyses and conclusions, quantitative analyses were performed on the "in-cell" and ex situ acquired images. **Figure 7** presents the different metrics used to quantify the electrode cracking patterns for both formulations measured in cell after 1, 5 and 25 cycles. The combination of both magnifications allows precise quantification of the crack pattern, which is labeled in two parts: (*i*) the macro-cracks (>0.65 µm in size) separating the islets of active material in a volume of 417 × 417 × 150 µm^3 and (*ii*) the micro-cracks in a volume of 25 × 25 × 25 µm^3 (>0.1 µm in size) located in the islets (see Figure S5 (Supporting Information) for more details on their estimation). These magnifications allow the calculation of crack volume fraction (Figure 7a), width distribution (Figure 7b), and network interconnectivity (Figure 7c) at both the electrode and interparticle scales. Additionally, the total electrode porosity can be determined by the sum of the pore/crack volume fractions measured at both micro- ($\varepsilon_{\text{crack}}{}^{(>0.65\ \mu\text{m})}$) and nano- ($\varepsilon_{\text{pore/crack}}{}^{(>0.1\ \mu\text{m})}$) scales according to Equation (3):

$$\varepsilon_{\text{electrode}} = \varepsilon_{\text{crack}}{}^{(>0.65\ \mu\text{m})} + \varepsilon_{\text{pore/crack}}{}^{(>0.1\ \mu\text{m})} \tag{3}$$

The total electrode porosity (and crack volume fraction) is rather stable during cycling for the formulation with Zn whereas it is constantly decreasing for the reference. The latter's porosity loss is estimated to be around −16%^{v} after 25 cycles. At the same state of aging for the formulation with Zn, the porosity is higher than at the pristine state (+7%^{v}). The evolution of the different cracking patterns during cycling is also striking. Their crack volume fractions generally follow the same trend as the volume fraction of their porosity. Specifically, for the formulation with Zn, the volume fraction of cracks in and between the islets remains fairly constant, with values always greater than 23%^{v}. This implies that most of the electrode porosity is still composed of these cracks after the 25th cycle. In fact, after the large decrease in crack width observed at the 1st cycle, the mean width of cracks between (and within) the islets stays constant, i.e., 1.4 (1.1) µm and 1.5 (0.9) µm at the 5th and 25th cycles, respectively (Figure 7b). These observations are illustrative of a breathing mechanism in the electrode microstructure with stable mechanical properties, leading to mitigated irreversible thickness expansion as already mentioned (Figures 3c and 4c). In contrast, the crack volume fraction and mean width between the islets decrease significantly more for the reference formulation. This underlines the fact that this electrode porosity is mainly composed of large pores able to withstand the clogging due to irreversible electrode deformation while smaller cracks cannot. Note that there could also be a limitation coming from the measurement precision restricting the segmentation to cracks >0.1 µm. The crack volume fractions measured within the islets by nano-tomography are indeed higher than between the islets for the reference formulation, especially at the 25th cycle. This could be explained through a two-step process. First, there is a general shrinkage of the crack

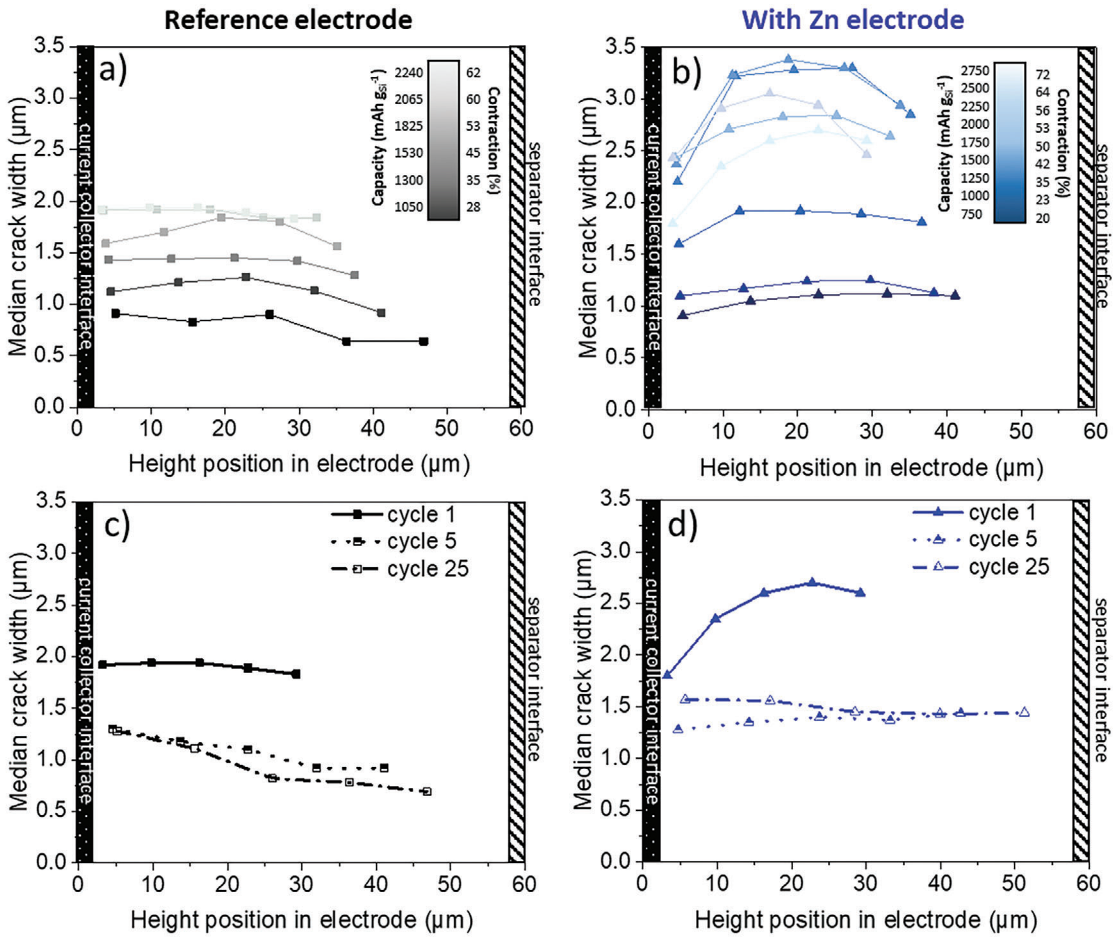

Figure 8. Evolution of the crack median width along the electrode's height during the a,b) 1st delithiation from operando-interrupted measurements and after further cycling from "in-cell" measurements c,d) for the (a,c) reference (in black) and (b,d) with Zn (in blue) formulations.

network between and inside the islets during the five first cycles. This is followed by a nearly complete closure of the large cracks between the islets (their volume fraction becomes insignificant at 1.5%^{v}) and associated increase of smaller cracks in the electrode bulk, up to 18%^{v}, as the large cracks turned into smaller ones. This also results in a slightly increasing mean width of the micro-cracks, from 427 nm (1st cycle) to 617 nm after the 25th cycle (Figure 7b). Finally, the overall crack pattern corresponds to a crumbled microstructure for the reference electrode.

It is visually clear that the Zn additive helps maintain the interconnectivity of the crack network as depicted in Figure 5. This is also supported by the measured values of the interconnectivity for the large cracks separating the islets which are far greater and more stable (82, 74, and 81% after 1, 5, and 25 cycles) as compared to the reference (68, 26, and 1.5%) formulation (Figure 7c). When investigating at higher resolution, the interconnectivity of the islets is still highest and most stable with the Zn additive. For the reference formulation, it decreases between cycle 1 and 5 from 83 to 61% before increasing back to 87% when the micro-crack (>0.1 µm) volume fraction increases due to the macro-cracks (>0.65 µm) clogging. It is assumed that after longer cycling, this micro-crack volume fraction will keep decreasing for the standard formulation due to continuous irreversible volume expansion and SEI formation as already discussed in detail in literature.[31,32] We can assume that this trend will be mitigated by the Zn additive, which presents the highest electrode microstructure resiliency to mechanical solicitation from repetitive cycles of expansion/contraction. This is also supported by the higher maximum mechanical cohesion and stiffness previously reported for the formulation with Zn.[12] Also, no delamination of the electrode coating has been observed for any of the studied formulations after 25 cycles, though this cannot exclude its potential appearance with further cycling.[33]

Figure 8 presents the evolution of the median crack width along the electrode depth, during (a, b) the first delithiation and (c, d) after further cycling for both formulations. Major differences are evidenced from the very first appearance of cracks. In fact, after 28% electrode contraction, wider cracks (0.91 µm) are measured close to the current collector compared to near the separator interface (0.65 µm) for the reference electrode. The formulation with Zn conversely presents wider cracks (1.12 µm) close to the separator after reaching 20% contraction compared to 0.91 µm near the current collector. During electrode contraction, the crack width increases overall, but with wider cracks near the current collector for reference formulation and narrower ones for the formulation with Zn (Figure 8a,b). Note that the crack width distribution along the depth of the reference electrode at the end of the 1st cycle, i.e., at 62% electrode contraction, is more homogeneous with cracks slightly wider towards the current collector interface as compared to the surface (1.92 vs 1.83 µm). For the formulation with Zn, there is a greater disparity in crack width along the electrode depth. The cracks are significantly wider at the separator interface than at the current collector (2.7 vs 1.8 µm). Nonetheless, after a contraction of 53%, smaller cracks open as evidenced by the lowering of the median crack width (with an exception around the current collector interface). This trend is not seen on the reference formulation electrode where the newly formed cracks are of similar dimensions to the initial cracks. These results illustrate locally what was observed macroscopically with the crack surface over volume ratios. Moreover, for the reference electrode after the 5th and 25th cycles, this trend becomes progressively more pronounced with wider cracks toward the current collector interface. This implies a weaker bonding strength of the reference electrode material to the current collector together with more freedom to crack and eventually delaminate. Interestingly, for the formulation with Zn, the cracks are still wider near the electrode/separator interface than at the electrode/current collector interface after the 5th cycle, showcasing a stronger anchorage to it. It is only after the 25th cycle that the crack width distribution is reversed. Ultimately, this indicates a better resistance to delamination of the formulation with Zn. In fact, the binder reticulation is beneficial in preventing electrode delamination from the current collector as previously reported in an in situ X-ray nano-tomography experiment.[10] This is also supported by the ten times higher critical scratch load measured for the Zn^{2+} coordinated binder formulation as compared to the reference electrode.[12] An explanation lies in the fact that the corrosion of the copper current collector is favored at pH C 3, inducing the formation of strong Zn(II)–carboxylates bonds between the binder and the current collector, as well as throughout the electrode.[11]

2.2.3. SEI Evolution along Early Cycle Life

For the present electrode formulations, SEI formation accounts for most of the excess discharge capacity during the 1st cycle and the related irreversible capacity loss, as shown in our previous work.[12] In **Figure 9** and 3D rendering images obtained from nano-tomography analysis are shown for the electrodes in pristine state and after cycling (1st, 5th, and 25th) for both formulations. The SEI analysis was carried out at the islet scale with sub volume images of 25 µm in height and 25 µm in circular diameter that were extracted from the full volume reconstructed ($64 \times 64 \times 54$ µm^3), selected at approximately the same depth in the electrode. The fine structure of the electrodes is clearly visible in the image of the pristine state with discernable Si particles (median width of 0.4 µm) and graphene sheets (labeled in yellow) crossing the imaged volume. After cycling, the morphology of the electrode has drastically changed and particles are hardly discernable. However, some of the graphene sheets are still visible and maintain connection between the different islets of electrode materials by creating bridges across the cracks, highlighting their crucial role as a conductive additive in Si-based anodes. Also, the electrode microstructure has cracks and some material of intermediate density filling a part of the cracked area. This is evidenced in the greyscale value histograms illustrating the case of the reference formulation in the supplementary information (Figure S6, Supporting Information). An intermediate peak contribution is visible in the deconvolution of the histograms which increases during cycling. In the present images, due to very close material densities, no distinction can be made between the binder phase, partially de/lithiated silicon material, and the SEI formed during cycling (identified as the green labeled phase in Figure 9). In fact, a progressively increasing mixing of SEI along with dead silicon caused by the disrupted electron pathway is foreseen, as previously reported in the literature.[34,35] We segmented this phase through a random forest classifier-based machine-learning algorithm.[36] As stated previously, the measurable image resolution is estimated at ≈100 nm (≈4 times the voxel size), giving a confidence threshold for the size of the features analyzed in the images (Figure S5, Supporting Information). This means that no contribution smaller than this threshold value can be analyzed quantitatively (see supplementary information for details on the resolution and segmentation). The segmentation results, after thresholding on the minimum values, are highlighted in green in the 3D images of Figure 9a,b (and 2D slices of Figure S6, Supporting Information), and this fraction is labeled "SEI-rich phase," as it contains mostly SEI products. The estimated volume of the SEI-rich phase per gram of active material (estimated as a fraction of the total mass loading reported to the analyzed volume) and mean SEI-rich phase thickness (from local thickness measurements) are plotted in Figure 9c. After the 1st cycle, the volume of the SEI-rich phase formed represents 0.63 (with Zn) and 1.19 cm^3 $g_{Si}{}^{-1}$ (reference). Based on theoretical mass compositions of the electrode formulations, an estimation of the binder volume per unit of Si allows for relativizing the present calculations. Values of 0.13 and 0.15 cm^3 $g_{Si}{}^{-1}$ are calculated for the reference and with Zn formulations, respectively (see Supporting Information for the calculation details). Hence, the larger binder volume in the Zn electrode highlights even more the difference in the estimated values between the formulations. At this stage, no significant difference in terms of SEI-rich phase mean thicknesses is measured with 122 and 124 nm for the with Zn and reference formulations, respectively. However, the local distributions of the SEI-rich phase thicknesses are clearly different with larger dispersion in the case of the reference electrode (Figure 9d). In fact, a larger contribution above 200 nm is reported as compared to the electrode with Zn, hence a larger volume fraction of the SEI-rich phase in total. Note that a higher spatial resolution in the image, i.e., <100 nm, could allow for the quantification of thinner contributions and thus increase the differences between the formulations.

The electrode microstructure in the islets is getting denser as the cycling progresses, with reduced volume fraction of pores/cracks for the reference compared to the formulation with Zn. This densification corresponds in part to the SEI-rich phase increasingly filling the electrode porosity after repetitive breakage through cycles of Si particle expansion/contraction. This is supported by the increasing SEI-rich phase volumes measured, which is exacerbated in the case of the reference formulation with 1.73 and 2.49 cm^3 $g_{Si}{}^{-1}$ after the 5th and 25th cycles, respectively (Figure 9c). This corresponds to a global thickening of the

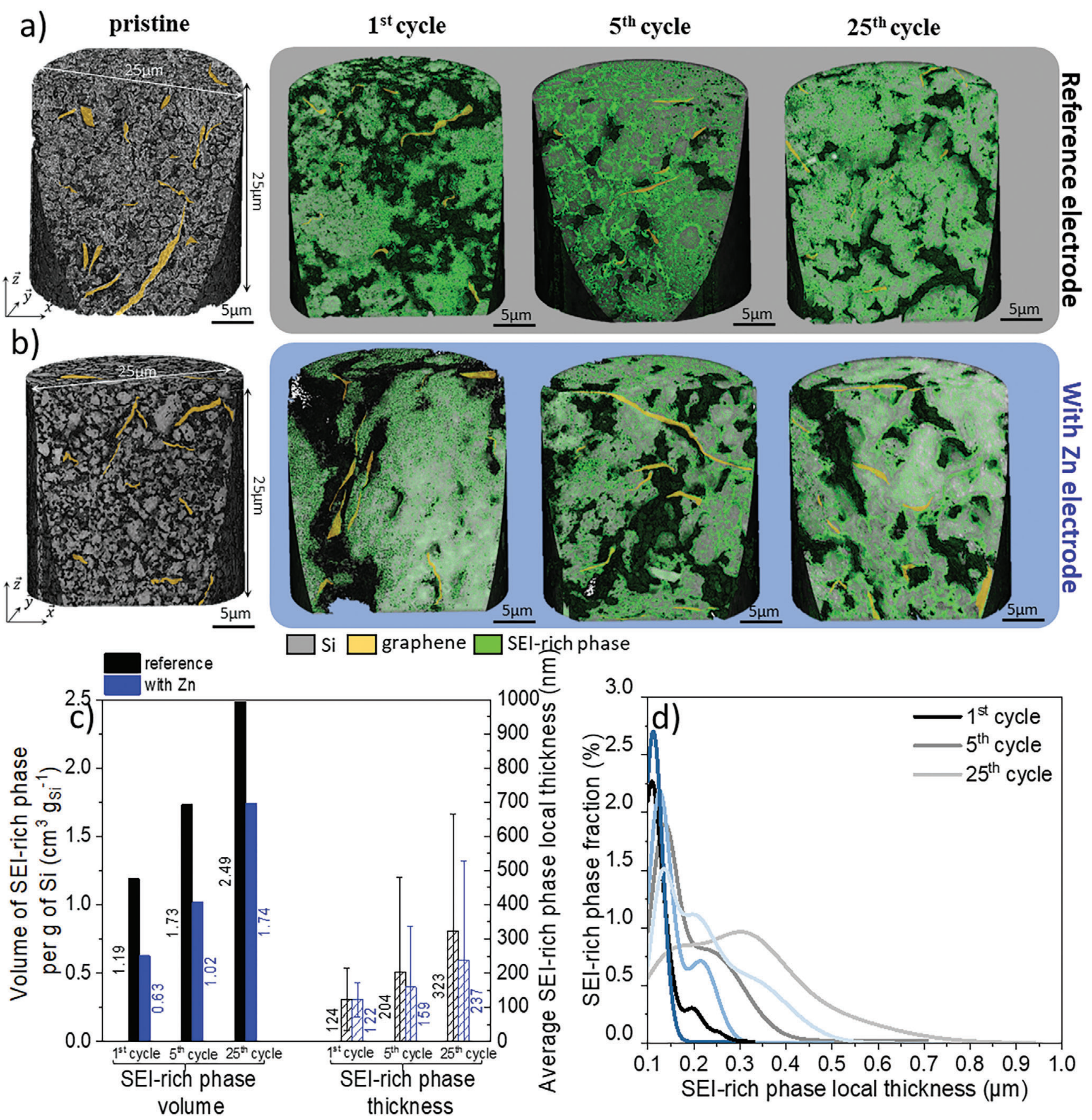

Figure 9. 3D rendering of X-ray nano-tomography reconstruction of the a) reference (in black) and b) with Zn (in blue) electrodes. From left to right: at the pristine state, end of 1st, 5th, and 25th cycle. The green label highlights the SEI-rich phase segmentation. c) SEI-rich phase volume per gram of active material along with average local thickness values, and d) SEI-rich phase local thickness distribution as a function of cycle number for the reference (in black) and with Zn (in blue) formulations.

SEI-rich phase with mean values evolving from 204 to 323 nm. Interestingly, the measured volume of the SEI-rich phase per gram of active material is lower for the electrode with Zn, with 1.02 and 1.74 $cm^3\ g_{Si}^{\ -1}$ at the 5th and 25th cycles, together with lower average thicknesses measured at these steps (159 and 237 nm, respectively). A more marked difference in the average SEI-rich phase local thickness is obtained when subtracting the binder contribution. In fact, average binder thicknesses of 32 and 37 nm covering the Si particles are calculated for the reference and with Zn formulations when supposing a uniform coverage of the particles. This difference suggests a denser and more uniform SEI with Zn, as previously observed by means of TEM measurements.[14] This hypothesis is also supported by the reduced standard deviation of the SEI-rich phase

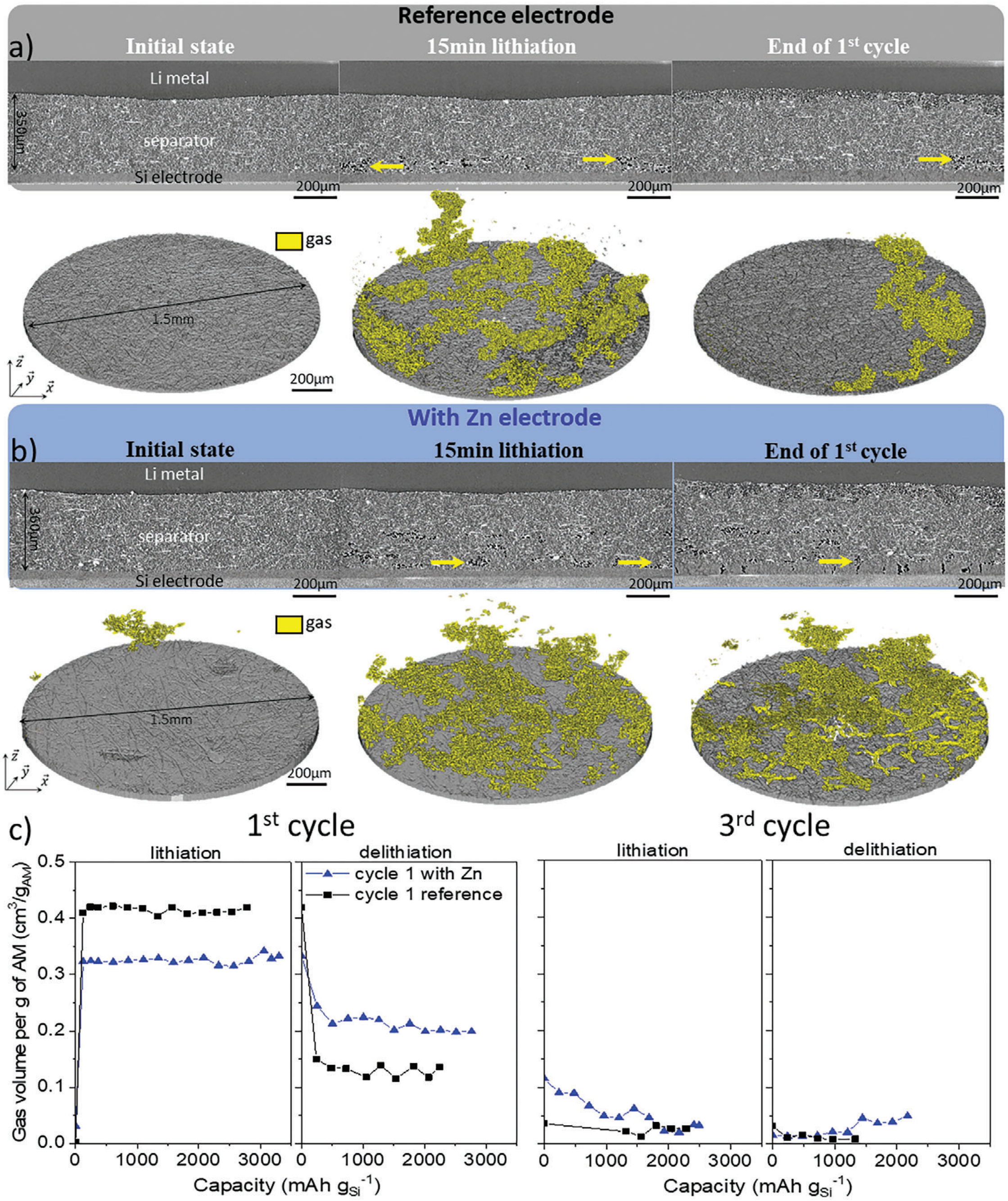

Figure 10. 2D cross section images and corresponding 3D rendering of gas formed in the a) standard formulation cell and b) the one with Zn. c) Volume of gas per gram of silicon generated by the reference and with Zn electrodes during the 1st (right) and the 3rd cycle (left).

local thickness measured for the electrodes with Zn (Figure 9c). This correlates with the lower irreversible capacity loss measured for the Zn-based formulation (Figure 2b). This is also in agreement with previous work, which indicates that coordinated binder acts, at least partially, as an artificial SEI.[12,14,35,37–39] The increase of the impedance due to continuous build up of SEI is expected to increase the polarization as seen in the voltage curves of Figure 2c,d. This may induce incomplete Si particle delithiation,[34] which in addition to the porosity filling by SEI, leads to irreversible electrode swelling and apparent decrease in the pore volume. These correlations are clearly observed in this study.

Changes also occur in the separator/electrolyte section of the half-cell as is visible in the cell cross section videos of the 1st and 3rd cycles (Videos S1 and S2, Supporting Information). **Figure 10** displays 2D cross section images of the half cells at specific cycling steps together with 3D renderings of the gas formed in the stack assembly (labeled in yellow) for the reference (a) and with Zn (b) electrodes. In this region, the separator fibers appear in white and the electrolyte in light grey. After the first 15 min of lithiation, some gas is observed in areas initially filled with electrolyte, mostly located near the electrode/separator interface. The volume of gas present inside the separator has been quantified and its evolution is presented in Figure 10c for the 1st and 3rd cycles. A drastic increase of the gas volume is seen right after the beginning of lithiation, from <0.01 to 0.43 and 0.32 $cm^3\ g_{Si}^{-1}$ for the reference and with Zn formulations. It is assumed that the gas formation observed is related to the electrolyte degradation and associated SEI formation as previously reported in literature.[10,40–42] In fact, the electrolyte volume depletions corresponding to the measured gas volumes are of −0.43 and −0.32 $mL\ g_{Si}^{-1}$ for the reference and with Zn formulations. If we consider that gases are formed mostly through two-electron electrochemical reactions,[43–47] it is possible to estimate the capacity corresponding to the gas volume measured (V_{gas}) based on Equation (4) derived from Faraday's law:

$$dQ\ [C] = n_{e-} \times \mathcal{F} = 2n_{gas} \times \mathcal{F} = \frac{2V_{gas} \times \mathcal{F}}{V_M} \qquad (4)$$

where n_{e-} and n_{gas} are the number of moles of electrons and gas exchanged, respectively, $\mathcal{F}$ the Faraday constant (96438 C mol^{-1}), and V_M the molar volume of a perfect gas (22.4 L mol^{-1}). In our case, we postulate that CO_2 is the main gas product resulting from FEC decomposition.[48,49] For the standard and with Zn formulations, the total volumes of gas are 0.014 and 0.011 mm^3 respectively, corresponding to 2.79 and $2.21\%^{v}$ of the separator porosity. Note that an underestimation of the generated gas volumes is possible as gas could be partially dissolved in the electrolyte and production could have occurred outside of the field of view. For the sake of comparison to the volume of the SEI-rich phase measured by nano-tomography (Figure 9c), the volume of SEI per gram of active material V_{SEI} corresponding to the volume of gas generated is estimated. We posit that the main degradation product accompanying the CO_2 gas formation is lithium carbonate.[48] Given that the number of moles of Li_2CO_3 (n_{Li2CO3}) is equal to the number of moles of gas (n_{gas}), we obtain Equation (5):

$$V_{SEI}\ \left[mm^3 g_{Si}^{-1}\right] = \frac{n_{Li_2CO_3} \times M_{Li_2CO_3}}{\rho_{Li_2CO_3} \times m_{Si}} \qquad (5)$$

with the molar mass and mass density of lithium carbonate being 73.89 g mol^{-1} and 2.11 g cm^{-3}, respectively. Hence, the corresponding V_{SEI} are 0.61 and 0.42 $cm^3\ g_{Si}^{-1}$ for the reference and with Zn formulations. This is in the same order of magnitude as the nano-tomography measurements (1.19 and 0.63 $cm^3\ g_{Si}^{-1}$ for the reference and with Zn formulations), but with lower values. This indicates that only a fraction of the reactions at play in the SEI formation lead to gas release despite the considerable volume of gas generated in the cell. In the present case, it represents 50 and 75% of the total SEI-rich phase volume estimated for the reference and with Zn formulations respectively. Comparatively, values of 0.25 (21%) and 0.18 (28%) $cm^3\ g_{Si}^{-1}$ for the reference and with Zn formulations have been estimated based on the equimolar formation of LiF and CH_2CHO.[50] The corresponding molar masses are 25.94 and 43 g mol^{-1} and the mass densities 2.64 and 2.01 g cm^{-3}, respectively.

Throughout the first lithiation, no displacements or significant increase of gas can be observed. Note that this observation differs from a previous report of a more continuous gas evolution while performing cyclic voltammetry at slow sweep rate (30 µV s^{-1}).[50] The gas volumes decline drastically after reaching the end of the lithiation, with a sudden drop to 0.15 and 0.24 $cm^3\ g_{Si}^{-1}$ for the reference and with Zn electrodes respectively. Note that this drop is measured only after 30 min of delithiation due to the temporal resolution chosen for this experiment. It is steadily stable until the cut off voltage of 1 V is reached for both electrodes, leading to 0.28 and 0.12 $cm^3\ g_{Si}^{-1}$ gas volume decrease after one cycle for the reference and with Zn formulations, respectively, as clearly highlighted by the 3D views of **Figure 10a,b**. In the cross-section images, the gas is visibly aspirated into the electrode cracks and disappears in the case of the reference while it remains visible in the electrode with Zn (Figure 10a,b). This clearly evidences the consumption of gas at the end of the lithiation, which is greater in the case of the reference electrode.

The amount of gas at the beginning of the 3rd cycle is even lower, with 0.04 and 0.11 $cm^3\ g_{Si}^{-1}$ remaining for the reference and Zn formulations, respectively (Figure 10c). A continuous decrease in gas volume is observed during lithiation, from 0.04 to 0.02 $cm^3\ g_{Si}^{-1}$ for the reference and from 0.11 to 0.03 $cm^3\ g_{Si}^{-1}$ for the formulation with Zn. There is a rather progressive decrease/increase of the gas volume over a given cycle, imitating the breathing mechanism of the electrode. This indicates that the gas formed in the early stage of the electrode cycling is progressively consumed during subsequent cycles. This agrees with previous studies from other groups on Si-based electrodes[40,41,51] with possible pathways for the consumption of CO_2 gas at low potential through its reduction to lithium oxalate and/or lithium carbonate.[41] In the literature, a beneficial synergy between the CO_2 formed and the FEC additive in the electrolyte has also been reported.[41,52–54] In sum, 0.28 and 0.12 $cm^3\ g_{Si}^{-1}$ of gas are consumed by the end of the 1st cycle and up to 0.42 and 0.28 $cm^3\ g_{Si}^{-1}$ in total by the end of the 3rd cycle for the reference and with Zn cells, respectively. Overall, this shows a mitigated gas release in the case of the formulation with Zn, along with a more progressive consumption of the gas "reservoir" over cycling, which is likely indicative of a more stable SEI formation and hence a better capacity retention.[51]

3. Conclusion

The addition of Zn(II) precursor to the poly(carboxylic acid) binder formulation enhances the electrode electrochemical performance and cycle life. The binder/cation couple forms a crosslinked coordinated binder that plays a key role toward enhanced mechanical and chemical stability of the electrode microstructure. This has been thoroughly investigated here from a microstructural point of view by the means of a complete workflow of analysis, combining operando, in situ and ex situ X-ray tomography measurements at different scales. In terms of mechanical stability, the binder reticulation through Zn-carboxylate bonds is effective in strengthening the electrode microstructure. This is illustrated qualitatively by the microstructural reversibility after each cycle of deformations, reducing the cumulated residual thickness expansion. In fact, the morphological deformations are limited and the cracking pattern is more resilient and efficient in accommodating large volume changes thanks to wider cracks and a better anchorage to the current collector. Overall, it helps prevent the electrode microstructure crumbling seen in the reference formulation, which very likely leads to many electrical disconnections and increased reactive surface. The latter promotes further electrolyte degradation and irreversible lithium loss through SEI formation as was directly measured by X-ray nano-tomography after 25 cycles. Another beneficial impact of the formulation with Zn with respect to the SEI also lies in the mitigation (in terms of volume and thickness) of its formation during the early cycle life. This is also supported indirectly by the reduced amount of gas released at that time as compared to the reference formulation. This is evidence that a coordinatively cross-linked CMC binder can play the role of an efficient artificial SEI layer. Finally, the synergetic and beneficial impact of CO_2 addition to the electrolyte combined with the zinc-based cross-correlated binder appears to be worth investigating in Si anodes.

4. Experimental Section

Material Preparation and Electrode Formulation: The Si powder used as active material was obtained by ball-milling commercial Si powder (325 mesh, 99.96%; Materion) using a HD-01 attritor (Union Process). The milling was performed under argon atmosphere for 20 h at 600 rpm with a ball-to-powder mass ratio of 10:1. The as-milled Si powder was composed of micrometric agglomerates as secondary particles (d_{50} ≈10 µm, S_{BET} ≈20 m^2 g^{-1}), with primary particles under 1 µm. The fraction of amorphous Si in the milled powder was estimated at 53.4% from Raman analysis and 63.6% from Rietveld refinement on the diffractogram.[14] The oxygen content determined by a LECO analyzer was ≈1% wt. To prepare the binder solution, first, a pH 3 buffer solution (0.171 M citric acid + 0.084 M KOH/NaOH) was obtained by dissolving citric acid (99%; Sigma–Aldrich) and KOH or NaOH salt (>98%; Sigma–Aldrich) in ultrapure water. Then, 5 mL of this buffer solution plus the volume of ultrapure water needed to reach 8.2 mL of solution was used to dissolve 160 mg of NaCMC (Mw ≈700 000 g mol^{-1}; D.S. 0.9; Sigma-Aldrich). The as-obtained solution was the reference binder (Zn/RCO2H = 0). To obtain the coordination binder, after complete and homogeneous NaCMC dissolution, the Zn(II) precursor was added in a single step and left under stirring until homogenized. For this study, the Zn(II) precursor used was: $ZnSO_4 \bullet 7H_2O$ (pure cryst.; Alfa Aesar). Its quantity was adjusted to reach a predefined theoretical molar coordination ratio of 0.22.[12] Then 160 mg of Si powder, 24 mg of graphene platelets used as conductive additive (xGnP M15 grade from XGSciences; average thickness ≈7 nm; average diameter = 15 µm; surface area ≈120–150 m^2 g^{-1}, according to supplier data) and 0.8 mL of binder solution were set in a vial with three balls (diameter = 9.5 mm), both made of silicon nitride. The ink was mixed using a Pulverisette 7 (Fritsch) planetary mixer for 1 h at 500 rpm. Then, for the two different formulations, i.e., with $ZnSO_4$ additive and without Zn, the as-prepared ink (22.3 and 21.5% solid fraction, respectively) was deposited using a 1 mL plastic pipette on Cu disks precut with a puncher (diameter = 3 mm; thickness ≈240 µm; 99.9%). Because one drop of ink was too much, the surplus was removed using a spatula, carefully avoiding spreading the ink on the other current collector side. Note that the Cu disks were flattened under a press (2.2 tons for 8 disks) prior for the coating step. This reduces the risk of irregular edges and the associated hardening during X-ray tomography acquisition, detrimental to reconstructed image quality and current collector/coating interface resolution. As-prepared electrodes were dried at room temperature for 12 h and subsequently further dried 2 h at 100 °C under vacuum (P ≈10 mbar). Electrodes were weighted using a MYA5.3Y.F scale (RADWAG) with a readability of 1 µg. Those with an active mass loading in the range of 1.75–2.0 mg_{Si} cm^{-2} were selected for further measurements. Then, they were dried again for 1 h at 100 °C under vacuum (P ≈10 mbar) prior to glove box transfer.

Electrochemical Cycling: For both formulations, electrodes were assembled in 3 mm diameter PFA Swagelok cells in an Ar filled glovebox (O_2 and H_2O < 1 ppm) in half-cell configuration as described in previous work.[21] A metallic Li disc (diameter = 3 mm; thickness = 380 µm; 99.9%; Aldrich) placed on a Cu current collector (diameter = 3 mm; thickness = 240 µm) served as both counter and reference electrodes. Two layers of glass microfiber were used as separator (grade GF/D; diameter = 3 mm; thickness = 670 µm; Whatman). The separator layers were soaked with 22.5 µL of electrolyte made of 1 M $LiPF_6$ in ethylene carbonate (EC) and dimethyl carbonate (DMC) (1:1, v:v) with an added 10% wt of fluoroethylene carbonate (FEC) (99.9%; Solvionic). Si electrodes were used for the cycling tests performed at room temperature using a multichannel VMP system (Biologic) in galvanostatic mode between 0.005 and 1 V (vs Li^+/Li). For the in situ/in-cell analyses, the C-rate was C/40 for the first cycle, C/20 for the next 5 cycles, and C/10 for the subsequent cycles (1C = 3579 mA g_{Si}^{-1}). For the operando-interrupted analysis, the C-rate was ≈C/8 (477 mA g_{Si}^{-1}) for the three first cycles investigated. Overall, electrodes performed as expected even considering the size-constrained tomography setup. This gives us confidence that the observations and conclusions drawn with this setup can be reliably transposed to the behavior in a conventional cell and with the deeper lithiation/delithiation enabled by slower C-rates (see Figure S4, Supporting Information). Prior to cycling, cells were rested 2 h at open circuit voltage (OCV). Cells were also relaxed at OCV for 10 s and 1 min after each discharge (lithiation) and charge (delithiation) steps, respectively.

X-Ray Micro-Tomography Measurements: X-ray micro-tomography analyses were performed at the TOMCAT beamline of the Swiss Light Source (SLS) at the Paul Scherrer Institut facility (Villigen, Switzerland). Using a monochromatic beam of 20 keV (2–3% bandwidth), a set of 1501 2D projections was acquired for each scan with 100 ms of exposure per projection along a 180° cell rotation, corresponding to a scan duration of ≈3 min. 3D tomographic volumes were collected at two different magnifications corresponding to isotropic voxel sizes of 0.16 and 0.65 µm, and reconstructed volumes of $417 \times 417 \times 352$ μm^3 or $1.54 \times 1.54 \times 1.30$ mm^3 respectively. These corresponded to two different magnifications for the optics of × 40 and × 10, respectively. An average resolution value of 0.65 µm was calculated for the high magnification micro-tomography images with a 0.16 µm voxel size (see Figure S7, Supporting Information). The tomographic volumes were reconstructed in 32-bit floating point representation from 2D projections using optimized software based on Fourier methods and an ImageJ plug-in user interface using a Paganin approach with a delta/beta value of 35.[55,56] The in situ "in-cell" analysis at different aging states, i.e., initial (after assembly), end of 1st cycle, 5th, and 25th cycles, were performed on separate batteries with high resolution (0.16 µm) for mitigating the risk of sample damaging while dismounting. The samples were cycled in advance and subsequently scanned within a few days after the sample had been cycled. This procedure was adopted to reduce the resting period between end of cycling and measurements. For the operando investigation, tomography scans were acquired every 15 min during the first 45 min of cycling, i.e., between 3 and 1 V, and every 30 min subsequently. These were performed for both the 1st and 3rd lithiation/delithiation cycle for the two formulations and using the two different magnifications. The combination of the two scans resulted in a total acquisition time of 7 min at each cycling state (including time to change the optics) during which the cell relaxed at OCV. The experiment was thus carried out in the "interrupted operando" mode.

X-Ray Nano-Tomography Analysis: The exact same half-cells previously selected for "in situ/in-cell" investigation using X-ray micro-tomography were subsequently dismantled in an Ar-filled glove box and the electrodes were retrieved and washed in DMC solution for 1 min twice, consecutively. Then, thin electrode fragments of lamella shapes (200 µm edge) were peeled off the electrode coating using a razorblade. The extracted samples were glued on top of glass capillaries (100 µm diameter) fixed onto a sample holder using an UV-polymerizing glue (Krylex) and finally sealed under Ar with surrounding PFA tubing. Nano-tomography acquisitions were performed ex situ on Si electrodes at their initial and cycled states (after 1, 5, and 25 cycles) at the ESRF ID16B beamline[57] using the holotomography technique.[58] Four tomographic scans with a pixel size of 25 nm were acquired using an incident X-ray beam with an energy of 17.5 keV and a flux of $2.6\ 10^{11}$ ph s^{-1} at four different sample-detector propagation distances. At each distance, 3203 projections, as well as 20 reference and 21 dark images were recorded on a PCO edge 5.5 camera (2560 × 2160 pixels^2) along a 360° rotation with an exposure time of 90 ms per angular position. The total acquisition time was ≈29 min per holotomography scan. 3D reconstructions were achieved in two steps: *(i)* phase retrieval calculation using an in-house developed octave script based on a Paganin-like approach using a delta/beta ratio of 207 for Si, and *(ii)* filtered backprojection reconstruction using ESRF software PyHST2.[59] Final volumes of 64 × 64 × 54 μm^3 with a voxel size of 25 nm in 32-bit floating point were obtained. Analyses were subsequently performed in a 25 × 25 × 25 μm^3 sub volume, representative of the electrode microstructure. Post-processing ring removal and 8-bit conversion was performed using a dedicated Matlab script.[60]

Image Analysis: In the case of micro-tomography acquisitions, image analyses were performed on the entire reconstructed 8-bit volume using the ImageJ software.[61] Details on the procedures for image segmentation and their quantitative analyses (dimensional change of the electrode, volume fraction, size distribution, interconnectivity of the segmented phases and crack growth) were presented in the Supporting Information. The different phases were segmented using thresholding on selected values that were estimated from the deconvolution of the grey value histogram based on an Otsu algorithm.[62] For the nano-tomography data sets analysis, the Ilastik open-source software was used for the segmentation of the SEI and cracking pattern, using a random forest classifier tool.[34,63] More details about this part were also available in the supplementary information.

Supporting Information

Supporting Information is available from the Wiley Online Library or from the author.

Acknowledgements

The authors thank the European Union's Horizon 2020 research and innovation program (Grant agreement No 814106, TEESMAT project) and the Natural Sciences and Engineering Research Council (NSERC) of Canada (grant RGPIN-2021-03374). The ESRF was thanked for provision of synchrotron radiation facilities (in-house beamtime IHMA117 at ID16B). The authors acknowledge the Paul Scherrer Institut, Villigen, Switzerland for provision of synchrotron radiation beamtime at the TOMCAT beamline X02DA of the SLS.

Conflict of Interest

The authors declare no conflict of interest.

Data Availability Statement

The data that support the findings of this study are available from the corresponding author upon reasonable request.

Keywords

binder, in situ, Li-ion batteries, silicon anode, X-ray tomography

Received: August 20, 2024
Published online:

[1] K. Feng, M. Li, W. Liu, A. G. Kashkooli, X. Xiao, M. Cai, Z. Chen, *Small* **2018**, *14*, 702737.
[2] L. Sun, Y. Liu, R. Shao, J. Wu, R. Jiang, Z. Jin, *Energy Storage Mater.* **2022**, *46*, 482.
[3] G. F. I. Toki, M. K. Hossain, W. U. Rehman, R. Z. A. Manj, L. Wan, J. Yang, *Ind. Chem. Mater.* **2024**, *2*, 226.
[4] G. G. Eshetu, E. Figgemeier, *ChemSusChem* **2019**, *12*, 2515.
[5] H. Wang, B. Wu, X. Wu, Q. Zhuang, T. Liu, Y. Pan, G. Shi, H. Yi, P. Xu, Z. Xiong, S.-L. Chou, B. Wang, *Small* **2022**, *18*, 2101680.
[6] S. Li, Y.-M. Liu, Y.-C. Zhang, Y. Song, G.-K. Wang, Y.-X. Liu, Z.-G. Wu, B.-H. Zhong, Y.-J. Zhong, X.-D. Guo, *J. Power Sources* **2021**, *485*, 229331.
[7] A. N. Preman, H. Lee, J. Yoo, I. T. Kim, T. Saito, S.-K. Ahn, *J. Mater. Chem. A* **2020**, *8*, 25548.
[8] T.-W. Kwon, J. W. Choi, A. Coskun, *Chem. Soc. Rev.* **2018**, *47*, 2145.
[9] C. Real Hernandez, A. Etiemble, T. Douillard, D. Mazouzi, Z. Karkar, E. Maire, D. Guyomard, B. Lestriez, L. Roué, *Adv. Energy Mater.* **2017**, *8*, 1701787.
[10] V. Vanpeene, J. Villanova, A. King, B. Lestriez, E. Maire, L. Roué, *Adv. Energy Mater.* **2019**, *9*, 1803947.
[11] D. Mazouzi, R. Grissa, M. Paris, Z. Karkar, L. Huet, D. Guyomard, L. Roué, T. Devic, B. Lestriez, *Electrochim. Acta* **2019**, *304*, 495.
[12] L. Huet, D. Mazouzi, P. Moreau, N. Dupré, M. Paris, S. Mittelette, D. Laurencin, T. Devic, L. Roué, B. Lestriez, *ACS Appl. Mater. Interfaces* **2023**, *12*, 15509.
[13] L. Huet, H. Houisse, N. Herkendaal, T. Devic, L. Roué, B. Lestriez, *Energy Technol.* **2023**, *11*, 2201483.
[14] L. Huet, P. Moreau, N. Dupré, T. Devic, L. Roué, B. Lestriez, *Small Methods* **2022**, *6*, 2200827.
[15] P. Pietsch, V. Wood, *Annu. Rev. Mater. Res.* **2017**, *47*, 451.
[16] T. M. M. Heenan, C. Tan, J. Hack, D. J. L. Brett, P. R. Shearing, *Mater. Today* **2019**, *31*, 69.
[17] E. Maire, P. J. Withers, *Int. Mater. Rev.* **2014**, *59*, 1.
[18] J. Scharf, M. Chouchane, D. P. Finegan, B. Lu, C. Redquest, M. C. Kim, W. Yao, A. Franco, D. Gostovic, Z. Liu, M. Riccio, F. Zelenka, J.-M. Doux, Y. S. Meng, *Nat. Nanotechnol.* **2022**, *17*, 446.
[19] D. Atkins, E. Capria, K. Edström, T. Famprikis, A. Grimaud, Q. Jacquet, M. Johnson, A. Matic, P. Norby, H. Reichert, J.-P. Rueff, C. Villevieille, M. Wagemaker, S. Lyonnard, *Adv. Energy Mater.* **2022**, *12*, 2102694.
[20] V. Vanpeene, J. Villanova, J.-P. Suuronen, A. King, A. Bonnin, J. Adrien, E. Maire, L. Roué, *Nano Energy* **2020**, *74*, 104848.
[21] V. Vanpeene, A. Etiemble, A. Bonnin, E. Maire, L. Roué, *J. Power Sources* **2017**, *350*, 18.
[22] B. Jerliu, E. Hüger, L. Dörrer, B.-K. Seidlhofer, R. Steitz, V. Oberst, U. Geckle, M. Bruns, H. Schmidt, *J. Phys. Chem. C* **2014**, *118*, 9395.
[23] Z. Karkar, T. Jaouhari, A. Tranchot, D. Mazouzi, D. Guyomard, B. Lestriez, L. Roué, *J. Power Sources* **2017**, *371*, 136.
[24] A. Tranchot, H. Idrissi, P.-X. Thivel, L. Roué, *J. Power Sources* **2016**, *330*, 253.
[25] M. N. Obrovac, L. J. Krause, *J. Electrochem. Soc.* **2007**, *154*, A103.
[26] X. Jiao, X. Yuan, J. Yin, F. B. Ajdari, Y. Feng, G. Gao, J. Song, *ACS Appl. Energy Mater.* **2021**, *4*, 10306.
[27] T.-W. Kwon, Y. K. Jeong, E. Deniz, S. Y. AlQaradawi, J. W. Choi, A. Coskun, *ACS Nano* **2015**, *9*, 11317.
[28] T. Boivin, B. Mathieu, W. Porcher, O. Gillia, *J. Electrochem. Soc.* **2024**, *171*, 010505.
[29] S.-Y. Lee, Y. Choi, S.-H. Kwon, J.-S. Bae, E. D. Jeong, *J. Ind. Eng. Chem.* **2019**, *74*, 222.
[30] T. Hildebrand, P. Rüesgsegger, *J. Microsc.* **1996**, *185*, 67.
[31] J. W. Choi, D. Aurbach, *Nat. Rev. Mater.* **2016**, *1*, 16013.
[32] A. Etiemble, A. Tranchot, T. Douillard, H. Idrissi, E. Maire, L. Roué, *J. Electrochem. Soc.* **2016**, *163*, A1550.
[33] C. Zhao, T. Wada, V. De Andrade, D. Gürsoy, H. Kato, Y. K. Chen-Wiegart, *Nano Energy* **2018**, *52*, 381.

[34] Y. He, L. Jiang, T. Chen, Y. Xu, H. Jia, R. Yi, D. Xue, M. Song, A. Genc, C. Bouchet-Marquis, L. Pullan, T. Tessner, J. Yoo, X. Li, J.-G. Zhang, S. Zhang, C. Wang, *Nat. Nanotechnol.* **2021**, *16*, 1113.
[35] J. Xiong, N. Dupré, P. Moreau, B. Lestriez, *Adv. Energy Mater.* **2022**, *12*, 2103348.
[36] A. Kreshuk, C. Zhang, in *Methods in Molecular Biology*, (Eds.: M. Bosch, E. Rebollo), Humana Press, New York, **2019**, *2040*, Ch. 21.
[37] C. C. Nguyen, T. Yoon, D. M. Seo, P. Guduru, B. L. Lucht, *ACS Appl. Mater. Interfaces* **2016**, *8*, 12211.
[38] K. W. D. K. Chandrasiri, C. C. Nguyen, B. S. Parimalam, S. Jurng, B. L. Lucht, *J. Electrochem. Soc.* **2018**, *165*, A1991.
[39] Z. Zheng, H. Gao, C. Ke, M. Li, Y. Cheng, D.-L. Peng, Q. Zhang, M.-S. Wan, *ACS Appl. Mater. Interfaces* **2021**, *13*, 53818.
[40] R. Jung, M. Metzger, D. Haering, S. Solchenbach, C. Marino, N. Tsiouvaras, C. Stinner, H. A. Gasteiger, *J. Electrochem. Soc.* **2016**, *163*, A1705.
[41] K. U. Schwenke, S. Solchenbach, J. Demeaux, B. L. Lucht, H. A. Gasteiger, *J. Electrochem. Soc.* **2019**, *166*, A2035.
[42] D. Aurbach, B. Markovsky, I. Weissman, E. Levi, Y. Ein-Eli, *Electrochim. Acta* **1999**, *45*, 86.
[43] D. Aurbach, A. Zaban, Y. Gofer, Y. E. Ely, I. Weissman, O. Chusid, O. Abramson, *J. Power Sources* **1995**, *54*, 76.
[44] H. Yoshida, T. Fukunaga, T. Hazama, M. Terasaki, M. Mizutani, M. Yamachi, *J. Power Sources* **1997**, *68*, 311.
[45] S. Geniès, R. Yazami, J. Garden, J. C. Frison, *Synth. Met.* **1998**, *93*, 77.
[46] K. Edström, A. M. Andersson, *J. Electrochem. Soc.* **2001**, *148*, A1100.
[47] R. Dedryvère, L. Gireaud, S. Grugeon, S. Laruelle, J.-M. Tarascon, D. Gonbeau, *J. Phys. Chem. B* **2005**, *109*, 15868.
[48] K. U. Schwenke, S. Solchenbach, J. Demeaux, B. L. Lucht, H. A. Gasteiger, *J. Electrochem. Soc.* **2019**, *166*, A2035.
[49] J. M. Martínez de la Hoz, P. B. Balbuena, *Phys. Chem. Chem. Phys.* **2014**, *16*, 17091.
[50] F. Jeschull, L. Zhang, L. Kondracki, F. Scott, S. Trabesinger, *J. Phys. Energy* **2023**, *5*, 025003.
[51] A. Schiele, B. Breitung, T. Hatsukade, B. B. Berkes, P. Hartmann, J. Janek, T. Brezesinski, *ACS Energy Lett.* **2017**, *10*, 2228.
[52] V. L. Chevrier, L. J. Krause, L. D. Jensen, C. Huynh, M. Triemert, E. L. Bowen, J. Thorson, *J. Electrochem. Soc.* **2018**, *165*, A2968.
[53] L. J. Krause, V. L. Chevrier, L. D. Jensen, T. Brandt, *J. Electrochem. Soc.* **2017**, *164*, A2527.
[54] E. J. Hopkins, S. Frisco, R. T. Pekarek, C. Stetson, Z. Huey, S. Harvey, X. Li, B. Key, C. Fang, G. Liu, *J. Electrochem. Soc.* **2021**, *168*, 030534.
[55] C. Hintermüller, F. Marone, A. Isenegger, M. Stampanoni, *J. Synchrotron Rad.* **2010**, *17*, 550.
[56] F. Marone, M. Stampanoni, *J. Synchrotron Rad.* **2012**, *19*, 1029.
[57] G. Martinez-Criado, J. Villanova, R. Tucoulou, D. Salomon, J.-P. Suuronen, S. Labouré, C. Guilloud, V. Valls, R. Barrett, E. Gagliardini, Y. Dabin, R. Baker, S. Bohic, C. Cohen, J. Morse, *J. Synchrotron Rad.* **2016**, *23*, 344.
[58] P. Cloetens, W. Ludwig, J. Baruchel, D. Van Dyck, J. Van Landuyt, J. P. Guigay, M. Schlenker, *Appl. Phys. Lett.* **1999**, *75*, 2912.
[59] A. Mirone, E. Brun, E. Gouillart, P. Tafforeau, J. Kieffer, *Nucl. Instrum. Meth. B* **2014**, *324*, 41.
[60] A. Lyckegaard, G. Johnson, P. Tafforeau, *Int. J. Tomo. Stat.* **2011**, *18*, 1.
[61] J. Schindelin, I. Arganda-Carreras, E. Frise, V. Kaynig, M. Longair, T. Pietzsch, S. Preibisch, C. Rueden, S. Saalfeld, B. Schmid, J.-Y. Tinevez, D. J. White, V. Hartenstein, K. Eliceiri, P. Tomancak, A. Cardona, *Nat. Methods* **2012**, *9*, 676.
[62] Q. Cao, L. Qingge, P. Yang, *J. Sens.* **2021**, *3*, 4896853.
[63] S. Berg, D. Kutra, T. Kroeger, C. N. Straehle, B. X. Kausler, C. Haubold, M. Schiegg, J. Ales, T. Beier, M. Rudy, K. Eren, J. I. Cervantes, B. Xu, F. Beuttenmueller, A. Wolny, C. Zhang, U. Koethe, F. A. Hamprecht, A. Kreshuk, *Nat. Methods* **2019**, *16*, 1226.